$6p_{1/2,3/2}np$; $J=0,1,2$ autoionizing series in atomic barium

B. Carré, P. d'Oliveira, P. R. Fournier, and F. Gounand
Service de Physique des Atomes et des Surfaces, Centre d'Etudes Nucléaires de Saclay, 91191 Gif-sur-Yvette CEDEX, France

M. Aymar
Laboratoire Aimé Cotton, Centre National de la Recherche Scientifique II and Université de Paris–Sud, 91405 Orsay CEDEX, France

(Received 17 April 1990)

We have investigated the $6p_{1/2,3/2}np$; $J=0$, 1, and 2 doubly excited, autoionizing series in atomic barium, that is, nine of the ten series of the $6pnp$ configuration, for n between 10 and 28. Experimental results are analyzed from two complementary points of view. First, we have studied the energy-level structure within a given n multiplet. Second, we have performed simple multichannel-quantum-defect-theory analysis of the $6p_{1/2,3/2}np;J$ series, for each J value. We find that the jk coupling scheme is the most appropriate for describing the resonance states in the long-range region.

I. INTRODUCTION

Numerous studies have now been devoted to the autoionizing doubly excited states of alkaline-earth atoms.[1–6] The doubly excited systems have revealed a wide spectrum of original features in their structure and properties. Among the most recent challenges, actually related, one can mention the excitation of $nln'l'$ double-Rydberg states, with high and comparable n,l and n',l' values,[6] the search for highly correlated configurations,[7] or the excitation of highly stable resonances.[8] The experimental studies make common use of the isolated core excitation (ICE) scheme,[9] in which the two electrons are successively optically excited. As a result, the excitation profile of the continuum in the resonance region presents itself as that of a quasibound state, with limited contribution of the direct underlying continuum. In barium, the $6pnl;J$ states have been particularly studied, since the $6s\rightarrow 6p$ transition involved in the ICE scheme is a strong, easily pumped transition.[10] In the work presented here, we have investigated the $6p_{1/2}np;J$ and $6p_{3/2}np;J$ states, for n between 10 and 28, J equal to 0, 1, and 2. The $6pnp$ configuration may be thought of as a relatively simple one, but was not studied until the recent work of Story, Yap, and Cooke on the $6p_{3/2}np;J$ series.[11] Accordingly, our results extend and complement those of Story, Yap, and Cooke. The noticeable interest of the $6pnp$ configuration is that it constitutes a manifold of autoionizing states involving a limited number of J components, four $6p_{1/2}np;J$ ($J=0,2\times 1,2$) and six $6p_{3/2}np;J$ series ($J=0,2\times 1,2\times 2,3$). Consequently, the experimental study can easily enough provide extended and consistent information on the manifold as a whole. In our experiment, nine of the ten J components are accessible, the $J=3$ state being excepted. This is in contrast with most of the studies of $6pnl$ configurations, for higher l: the latter should proceed through successive attempts, each concerned with a particular J value at a time.[12] The other advantage is that analysis of the experimental results can be global, including most of the J components for a number of n multiplets. Moreover, two complementary types of analysis can be performed, that were usually separately developed.[11] First, it is possible to analyze the energy spacings between the different J states, within a given n multiplet, in terms of spin-orbit and Slater integral parameters. Second, measurement of $6pnp;J$ series, for a given J, allows multichannel-quantum-defect-theory (MQDT) treatment of the data. In this paper, we make a simple attempt to associate in a consistent manner the former and latter types of analysis.

Experimentally, the ICE scheme is easily set up with only two laser excitation steps, as shown in Fig. 1. A first, uv photon excites the $6snp\ ^1P_1$ state, whose energy has been measured by Armstrong, Wynne, and Esherick;[13] a second photon excites the $6s\rightarrow 6p_{1/2,3/2}$ transition, in the 450–500 nm range. The $6p_{1/2,3/2}$ limits are at 62 296.46 and 63 987.32 cm^{-1}, respectively. Within the above ICE scheme, we have introduced a selective excitation of the different J states, by choosing appropriate combinations of laser polarizations. Because of the relatively simple situation, the dependence of the different transition moments on the angular momentum and light polarization can be computed. It allows discussion of the ion yield measurements, contributing to the tentatively global analysis proposed.

The organization of the paper is as follows: experimental technique and results are reported in Secs. II and III, respectively; analysis and discussion are in Sec. IV.

II. EXPERIMENT

The isolated core excitation scheme has already been introduced in Sec. I and Fig. 1. The experimental setup is schematically represented in Fig. 2. The barium effusive beam is produced out of an oven at 750 °C. The

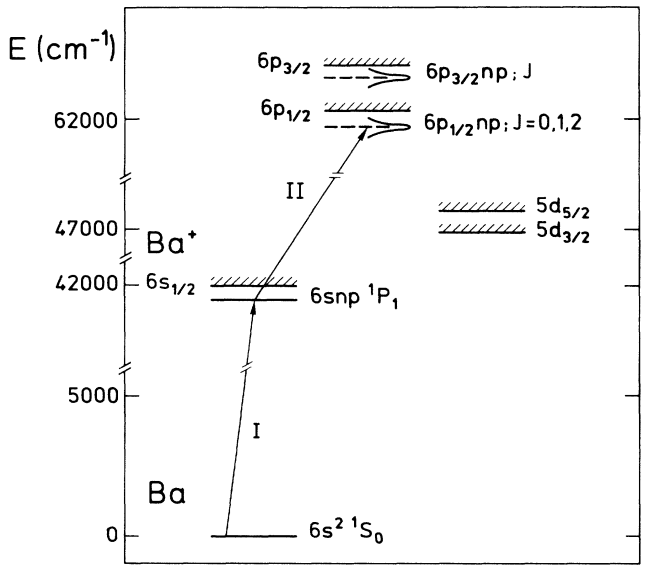

FIG. 1. Schematic of the isolated core excitation (ICE). Laser I in the range 250–240 nm excites the $6snp\ ^1P;J_i=1,M_i$ state; laser II excites either the $6p_{1/2}np;JM$ (500–490 nm) or the $6p_{3/2}np;JM$ resonance (460–450 nm). Ionization thresholds are at $6s_{1/2}$, 42 034.08 cm^{-1}; $6p_{1/2}$, 62 296.46 cm^{-1}; $6p_{3/2}$, 63 987.32 cm^{-1}. Combined polarizations of lasers I and II introduce selective pumping of J_iM_i intermediate and JM final states—see Sec. II.

oven aperture (0.5 mm in diameter) is overheated by about 100 °C to avoid condensation and formation of dimers. The interaction region is located at 3 cm from the oven aperture; the barium density is of the order of 10^9 cm^{-3}. The barium beam is stepwise excited by two counterpropagating laser beams, I and II, making angles of 45° and 135°, respectively, with the mean velocity of the atoms in the horizontal plane. Although Doppler shifts are of different signs for the two laser excitations, this configuration is very convenient for superimposing the beams in the interaction region. Excitation takes place between two plates of diameter 6 cm and 6 mm apart. A

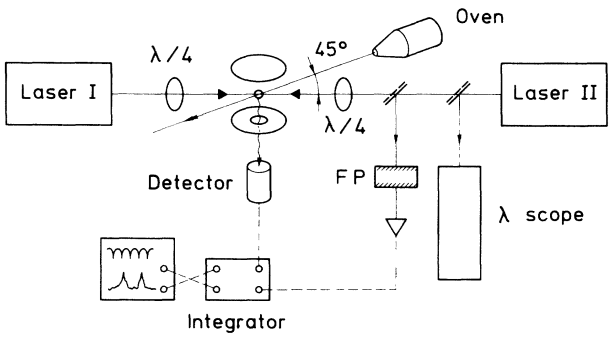

FIG. 2. Experimental setup. Laser II wavelength λ_{II} is calibrated using a Lambdascope device coupled with a Fabry-Pérot étalon (FP). Lasers I and II are polarized by means of λ/4 plates (additional polarizer is required in $L_{\parallel}$ configuration).

300-V voltage is applied 1 μs after the laser pulses for collecting the Ba^+ ions, a grid being mounted on the lower plate. The ions are detected with a MM2 Johnston electron multiplier after a 10-cm drift. The output current is integrated within a 3-ns time gate and over 10 to 100 laser pulses using a Stanford Research Systems boxcar integrator. The ion yield signal is finally recorded on a XY chart recorder, as a function of laser II wavelength. Four examples of Ba^+ ion yield spectra measured in the case of $6s^2\ ^1S_0 \rightarrow 6s26p\ ^1P_1 \rightarrow 6p_{1/2}26p;J$ excitation are displayed in Fig. 3; they are commented on further in the text.

Laser I is used for exciting the $6s^2\ ^1S_0 \rightarrow 6snp\ ^1P_1$ transition, with $n=10$ to 28, between $\lambda=254$ nm ($n=10$) and 238 nm ($n=28$). In this range, the energy of the $6snp\ ^1P_1$ intermediate step I is accurately known, within 0.01 cm^{-1}, from measurements in Ref. 13 [actually, we have found that it was much easier to excite the $6p_{1/2,3/2}13p;J$ states from the state labeled $5d_{5/2}4f_{5/2}$ in Ref. 13, at 40 736.81 cm^{-1}, rather than from the $6s13p\ ^1P_1$ state at 40 765.23 cm^{-1}; this suggests that the labelings of the

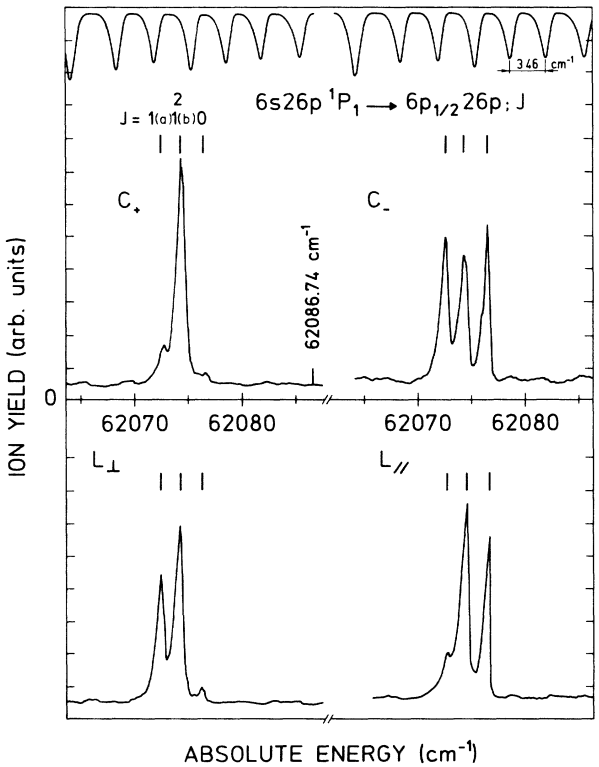

FIG. 3. Ba^+ ion yield spectra produced by the $6s26p\ ^1P_1,M_i \rightarrow 6p_{1/2}26p;JM$ excitation, as a function of λ_{II} (absolute energy scale), in the four cases of laser polarization: C_+, $\sigma^+\sigma^+$; C_-, $\sigma^+\sigma^-$; $L_\perp$, $\pi\pi^\perp$; $L_\parallel$, $\pi\pi$. Fringe pattern from the FP étalon and absolute energy reference are simultaneously recorded. The maximum ratio of resonant to nonresonant signal is larger than 10. Of the four J components [1(a),1(b),2,0] of the multiplet, $J=1$(b) and $J=2$ are not resolved. Even in that case, use of coefficients in Table I allows unambiguous assignment of the structures.

states in Ref. 13 should presumably be permuted]. Lower n ($n=9$) or higher n states ($n>28$) cannot be easily pumped in our experimental conditions. Laser I chain consists in an excimer pump (Lambda Physics—100 mJ/pulse) pumping a tunable dye (Lambda Physics 3002) working with coumarin C102, further doubled in a beta-barium-borate (BBO) crystal. Output energy after attenuation and doubling is typically 50 μJ/pulse for a pulse duration of 20 ns. The laser beam is focused in the interaction region through a telescope (beam waist of 0.1 mm); the corresponding intensity of 10^6–10^7 W cm^{-2} produces significant pumping and measurable photoionization of the $6snp\ ^1P_1$ state. Laser II is used for exciting the $6snp\ ^1P_1 \rightarrow 6p_{1/2}np;J$ or $6p_{3/2}np;J$ transition to autoionizing resonances. Laser II chain consists in N_2-laser pumping a tunable dye. The first transition between 500 and 490 nm is pumped using an appropriate admixture of coumarin C500 and C102. The second transition between 460 and 450 nm is pumped with C47. The energy output is of typically 70 μJ/pulse for a pulse duration of 10 ns; the spectral linewidth is 0.70 cm^{-1}. The same focusing as for laser I and use of neutral density filters lead to a working intensity of 10^5–10^6 W cm^{-2}. For this moderate intensity, resonance profile can be measured without being affected by power broadening and resonance saturation.

The accurate calibration of laser II wavelength, λ_{II}, between 500 and 450 nm is obtained from two complementary measurements, which are illustrated in Fig. 2. First, a fraction of laser II beam is transmitted through a Fabry-Pérot étalon (free spectral range of 3.46 cm^{-1}). The fringes of the intensity pattern are recorded simultaneously with the ion yield, as a function of λ_{II}—see Fig. 3. Secondly, another fraction of the beam is diverted into a "Lambdascope" device, which provides series of absolute energy measurements, e.g., in Fig. 3, at 62 086.74 cm^{-1}. The principle of the Lambdascope has been reported in Ref. 14. As a result, λ_{II} is measured with an energy accuracy of 0.05 cm^{-1}.

In order to introduce a selective pumping of the J component in the resonance state, we have used combined polarized lights for both steps I and II. Initially linear, perpendicular polarizations of lasers I and II are transformed into right- or left-circular polarizations by means of $\lambda/4$ plates installed in both beams, without changing their intensity. The configurations produced are therefore (i) linear perpendicular $\pi\pi^{\perp}$, which is labeled $L_{\perp}$; (ii) $\sigma^+\sigma^+$ right-right-circular with respect to the same propagation axis, labeled C_+; (iii) $\sigma^+\sigma^-$ right-left circular, labeled C_-. A fourth $\pi\pi$ linear parallel configuration, labeled $L_{\parallel}$, is produced with use of an additional polarizer after the $\lambda/4$ plate, on laser beam II. Since the intensity is reduced, the ion yield measurements in $L_{\parallel}$ require an appropriate normalization to those in the three previous configurations. In the four configurations used, the rate of polarization is about 95% of the total intensity for each beam. The first excitation step populates either $6snp$; $J_i=1$, $M_i=0$ ($L_{\parallel}$,$L_{\perp}$), or $M_i=1$ level (C_+,C_-), the transition amplitude being independent of M_i. The second step introduces a selective pumping of the different J components, according to the selection rules in the expression of the squared transition moment:[15]

$$|\langle 6snp;J_iM_i|\mathbf{r}\cdot\boldsymbol{\epsilon}|6pnp;JM\rangle|^2=\left[\sum_q \epsilon_q \begin{pmatrix} J_i & 1 & J \\ M_i & q & -M \end{pmatrix}\right]^2 |\langle 6snp;J_i\|rC^{(1)}\|6pnp;J\rangle|^2 , \quad (1)$$

where the ϵ_q are the real standard components of the laser II polarization. The angular factors multiplying the reduced matrix element are listed in Table I for the different polarization configurations. Note that they allow comparison of the transition probabilities between two polarization configurations but for the same J value.

Each of the four spectra in Fig. 3 corresponds to a particular combination of laser polarizations, i.e., $C_+,C_-,L_{\perp},L_{\parallel}$, respectively. Using the coefficients in Table I, we can, in most cases, unambiguously assign a J value to the observed structures. Some measurable deviations from the variation predicted are observed, when the expected value is a small or zero value, e.g., in Fig. 3, for $J=1$ in C_+ and $L_{\parallel}$, for $J=0$ in C_+ and $L_{\perp}$. This is attributed to the residual polarization of the light introducing residual excitation, which can be of the same order of magnitude as the one produced by the dominant polarization. Definite assignment of some of the J components, when not clearly resolved, has required analysis of the residual excitation.

TABLE I. Angular factors in the squared transition moment $|\langle 6snp;J_iM_i|\mathbf{r}\cdot\boldsymbol{\epsilon}|6pnp;JM\rangle|^2$—see Eq. (1)—as a function of laser polarizations and J value. The table allows comparison of the ion yield magnitude for different polarizations but for the same J value.

J	C_+	C_-	$L_{\parallel}$	$L_{\perp}$
0	0	1/3	1/3	0
1	0	1/6	0	1/6
2	1/5	1/30	2/15	1/10

In the conditions of isolated core excitation, spectra in Fig. 3 show that the nonresonant photoionization remains much weaker, by a factor of about 10, than the resonant one. The excitation profile of a resonance state is essentially Lorentzian, centered at energy E that we call the resonance energy, and with a full width at half maximum (FWHM) Γ. Width is measurable providing it is larger than 0.3 cm^{-1}, i.e., not too small with respect to the laser linewidth. Then, energy positions and widths are measured with the same accuracy of 0.3 cm^{-1}. The corresponding uncertainty on the $\nu_{1/2},\nu_{3/2}$ effective quantum numbers varies as $2\nu^3\Delta E/R$ ($R=109\,736.87$ cm^{-1}

is the Rydberg constant for barium), from 0.001 ($n=10$) to 0.02 ($n=28$).

III. RESULTS

Two sets of measurements have been performed, of the $6p_{1/2}np;J=0,1,2$ and $6p_{3/2}np;J=0,1,2$ autoionizing series, respectively, for n varying between 10 and 28. As we have mentioned, the $6p_{3/2}np$; $J=0$, 1, and 2 series have been already studied by Story, Yap, and Cooke[11] for n between 14 and 21. For these series, our results extend—a new $J=1$ series is measured—and somewhat complement the results in Ref. 11. The presentation of our results aims at offering a global view of the $6pnp$ configuration; it supports the simple, but tentatively global, analysis of Sec. IV. Energy positions, effective quantum numbers and widths of the autoionizing series are reported in Table II ($J=0$), parts (a) and (b) of Table III ($J=1$), and Table IV ($J=2$). In the case of two $6pnp;J$ series having the same limit, for $J=1$ or 2, the series of lowest energy is labeled (a), the second one is labeled (b).

The relative position of the $6p_{1/2}np;J$ and $6p_{3/2}np;J$ series below $6p_{1/2}$ threshold can be followed in the tables (the energy position of the $6p_{3/2}9p$ multiplet is extrapolated from the measured values at higher n). The significant interaction between the $6p_{1/2}np;J$ and $6p_{3/2}n'p;J$ series below the $6p_{1/2}$ limit clearly appears on the Lu-Fano plots of $\nu_{1/2}$ as a function of $\nu_{3/2}$ in Figs. 4–6, for $J=0$, 1, and 2, respectively. The solid lines displayed in the figures result from a MQDT fit which is developed in Sec. IV; in the present section, the graphs only serve as guidelines for reading the plots of experimental points.

Another, direct illustration of the interaction between the two $6p_{1/2}np;J$ and $6p_{3/2}n'p;J$ series is given in the spectra in Fig. 7. Spectrum (a) is measured with $L_{\parallel}$ polarizations, when the $6s11p\ ^1P_1$ initial state is populated, and λ_{II} wavelength scanned in the range 430–450 nm, in the vicinity of the $6s11p\rightarrow 6p_{3/2}11p$ transition. Besides the structures which can be assigned to the $6p_{3/2}11p$ multiplet, the spectrum exhibits a number of additional peaks labeled $(n;J)$. Namely, in Fig. 7, they correspond to the excitation of the $6p_{1/2}20p;J=2$ and $6p_{1/2}np;J=0$ resonance states for $n=21,22$. Actually, the $J=0$ states were observed, in the same conditions, for $n=18$ to 24, as were the $6p_{1/2}np;J=1$ states for C_- or $L_{\perp}$ polarizations. Thus the spectrum gives direct evidence of an admixture of $6p_{3/2}11p$ character in the $6p_{1/2}np;J$ states. We note in Figs. 4–6 that these states fall into the perturbed region of the Lu-Fano plots. Figure 6 also shows that, while the $6p_{1/2}20p;J=2$ state is strongly perturbed, the other $J=2$ states should be less mixed, and actually are not excited in spectrum (a) in Fig. 7. Now, spectrum (b) is measured with $L_{\parallel}$ polarizations, in the case of a direct excitation $6s22p\rightarrow 6p_{1/2}22p$ of the $n=22$ multiplet, i.e., λ_{II} in the vicinity of 500 nm. We note that spectrum (b) reduces to the single $J=2$ structure, the $J=0$ structure which was produced in spectrum (a) has disappeared. Besides the channel mixing in the final state, part of the contrast between the two paths should also involve the $(^1P,^3P)$ mixing in the $6snp;J_i=1$ initial state, for $n=18$ to 24.[16]

A. The $6p_{1/2}np;J$ series

1. $J=0$

Table II and the Lu-Fano plot in Fig. 4 show the importance of the interaction between the two

TABLE II. Resonance energies, effective quantum numbers, and widths (FWHM) for the $6p_{1/2}np;J=0$ and $6p_{3/2}np;J=0$ series. The width of the $6p_{1/2}np;J=0$ states is smaller than 0.3 cm^{-1}, i.e., not measurable, for $n\geq 12$.

	$6p_{1/2}np;J=0$			$6p_{3/2}np;J=0$		
n	E (cm^{-1})	$\nu_{1/2}$	Γ (cm^{-1})	E (cm^{-1})	$\nu_{3/2}$	Γ (cm^{-1})
10	59 478.7	6.241	1.0	61 338.2	6.436	1.3
11	60 116.3	7.095	2.4	61 985.8	7.405	1.8
12	60 694.0	8.278		62 432.0	8.400	24.3
13	61 005.2	9.219		62 741.0	9.383	17.8
14	61 249.1	10.236		62 967.9	10.375	14.3
15	61 445.6	11.357		63 137.5	11.363	12.4
16	61 569.1	12.283		63 268.1	12.353	7.4
17	61 671.7	13.253		63 370.9	13.343	5.5
18	61 754.5	14.230		63 453.5	14.337	4.0
19	61 822.1	15.210		63 520.2	15.328	4.0
20	61 877.1	16.176		63 575.6	16.325	3.3
21	61 922.5	17.130		63 621.5	17.319	2.5
22	61 958.5	18.018		63 659.9	18.308	
23	62 009.0	19.539		63 692.3	19.286	3.3
24	62 033.3	20.421		63 721.1	20.302	1.3
25	62 056.2	21.373		63 745.4	21.296	1.1
26	62 076.7	22.345		63 766.5	22.294	0.6
27	62 094.7	23.320		63 784.9	23.285	
28	62 111.0	24.325		63 801.5	24.303	

TABLE III. Resonance energies, effective quantum numbers, and resonance widths (FWHM) for the (a) $6p_{1/2}np$;$J=1$(a) and 1(b) series and (b) $6p_{3/2}np$;$J=1$(a) and 1(b) series.

(a) $6p_{1/2}np$;$J=1$(a) and 1(b) series

	$6p_{1/2}np$;$J=1$(a)			$6p_{1/2}np$;$J=1$(b)		
n	E (cm^{-1})	$\nu_{1/2}$	Γ (cm^{-1})	E (cm^{-1})	$\nu_{1/2}$	Γ (cm^{-1})
10	59 353.5	6.106	25.9	59 439.7	6.198	8.0
11	60 139.4	7.133	2.4	60 200.4	7.236	0.8
12	60 630.1	8.115	5.4	60 670.0	8.214	1.0
13	60 978.8	9.126	3.3	61 004.6	9.216	
14	61 229.8	10.143	2.1	61 252.8	10.254	0.3
15	61 410.5	11.129	1.5	61 426.1	11.228	0.1
16	61 549.6	12.122	2.5	61 561.7	12.221	0.1
17	61 660.1	13.132	6.9	61 667.8	13.212	1.4
18	61 747.9	14.143	2.0	61 753.2	14.212	2.2
19	61 820.2	15.180		61 825.7	15.267	1.2
20	61 873.9	16.116	0.5	61 876.3	16.161	≤ 0.1
21	61 922.5	17.130		61 928.9	17.279	
22	61 963.2	18.147		61 966.7	18.242	
23	61 996.6	19.128	0.3	61 999.4	19.221	
24	62 026.0	20.143	0.7	62 028.3	20.228	
25	62 050.8	21.137	0.3	62 053.0	21.229	
26	62 072.6	22.142	0.3	62 074.4	22.230	
27	62 091.5	23.139	0.3	62 093.0	23.226	
28	62 108.2	24.146	0.3	62 109.6	24.232	

(b) $6p_{3/2}np$;$J=1$(a) and 1(b) series

	$6p_{3/2}np$;$J=1$(a)			$6p_{3/2}np$;$J=1$(b)		
n	E (cm^{-1})	$\nu_{3/2}$	Γ (cm^{-1})	E (cm^{-1})	$\nu_{3/2}$	Γ (cm^{-1})
10	61 050.1	6.112	5.4	61 166.6	6.237	0.8
11	61 811.1	7.101	1.4	61 898.7	7.248	0.6
12	62 321.1	8.115	4.8	62 373.0	8.245	6.2
13	62 666.7	9.116	4.5	62 702.4	9.242	5.6
14	62 915.5	10.119	2.8	62 941.9	10.245	4.7
15	63 099.5	11.120	2.2	63 119.7	11.246	3.8
16	63 240.5	12.121	1.7	63 255.3	12.244	2.4
17	63 350.2	13.124	1.5	63 362.2	13.250	1.7
18	63 437.2	14.124	1.5	63 447.1	14.252	1.3
19	63 507.6	15.124	1.3	63 515.9	15.258	1.5
20	63 565.3	16.126	1.5	63 572.2	16.260	1.0
21	63 613.1	17.124	1.1	63 618.9	17.258	0.9
22	63 653.4	18.127	1.3	63 658.3	18.264	0.7
23	63 687.0	19.116	1.5	63 690.2	19.219	2.4
24	63 716.2	20.118	1.7	63 719.1	20.228	1.6
25	63 741.4	21.123	0.9	63 744.0	21.239	1.0
26	63 763.5	22.140	1.0	63 765.1	22.223	1.6
27	63 782.3	23.134	1.0	63 783.7	23.217	1.2
28	63 798.9	24.131	1.0	63 800.3	24.225	

$6p_{1/2}np$;$J=0$ and $6p_{3/2}n'p$;$J=0$ series. Actually, most of the states between $n=10$ and 25 are perturbed. The "unperturbed" value of the $\delta_{1/2}^{J=0}$ quantum defect is approximately that for $n=25$ to 28, i.e., 3.75. Except for the first two states, the resonance widths are found smaller than 0.7 cm^{-1} and thus not measurable. They are also smaller than the energy spacing between two J components.

2. $J=1$

The two $6p_{1/2}np$;$J=1$(a) and 1(b) series in part (a) of Table III interact with the two corresponding $6p_{3/2}n'p$;$J=1$(a) and 1(b) series. Compared to Fig. 4, the interaction illustrated by the Lu-Fano graph in Fig. 5 is not as strong as in the $J=0$ case, both curves presenting portions of constant quantum defects, $\delta_{1/2}^{J=1(a)}=3.86$ and

TABLE IV. Resonance energies, effective quantum numbers, and widths for the $6p_{1/2}np;J=2$ and $6p_{3/2}np;J=2$(a) and 2(b) series. Energy and width of the $6p_{3/2}np;J=2$(a) state are not determined for $n=20$ and 21, since the corresponding structure is hardly measurable—see Sec. III B 4.

	$6p_{1/2}np;J=2$			$6p_{3/2}np;J=2$(a)			$6p_{3/2}np;J=2$(b)		
n	E (cm^{-1})	$\nu_{1/2}$	Γ (cm^{-1})	E (cm^{-1})	$\nu_{3/2}$	Γ (cm^{-1})	E (cm^{-1})	$\nu_{3/2}$	Γ (cm^{-1})
10	59 438.5	6.197	34.2	61 086.7	6.151	9.0	61 154.0	6.223	17.3
11	60 196.5	7.229	10.9	61 844.3	7.156	4.8	61 889.3	7.232	8.1
12	60 666.1	8.204	9.8	62 335.3	8.150	4.0	62 367.9	8.232	11.0
13	61 004.6	9.216	9.3	62 682.6	9.171	3.3	62 697.3	9.223	7.1
14	61 249.1	10.236	4.9	62 925.6	10.166	2.8	62 937.4	10.223	4.8
15	61 424.9	11.221	2.6	63 106.2	11.160	2.5	63 116.2	11.224	4.6
16	61 560.6	12.211	3.2	63 244.9	12.157	1.9	63 252.8	12.223	3.0
17	61 668.1	13.215	4.4	63 353.5	13.158	1.4	63 359.7	13.222	2.7
18	61 754.0	14.223	2.4	63 440.3	14.164		63 445.4	14.230	2.5
19	61 822.1	15.210	1.5	63 510.0	15.162		63 514.1	15.228	2.1
20	61 876.3	16.161	1.6				63 570.6	16.228	2.0
21	61 927.2	17.240	1.2				63 617.6	17.227	1.9
22	61 966.7	18.242	0.9	63 654.6	18.161	2.4	63 656.7	18.220	1.6
23	61 999.4	19.221	0.9	63 688.2	19.153	2.4	63 690.1	19.215	1.4
24	62 028.3	20.228	0.7	63 717.1	20.150	2.8	63 719.0	20.221	1.4
25	62 053.0	21.229	0.4	63 742.6	21.174	1.5	63 743.7	21.222	0.9
26	62 074.4	22.230	0.3	63 763.9	22.164	1.6	63 765.1	22.223	1.1
27	62 093.0	23.226	0.3	63 782.8	23.166	1.4	63 783.7	23.217	1.0
28	62 109.6	24.232	0.4				63 800.3	24.225	

$\delta_{3/2}^{J=1(b)}=3.77$. In the average, the $6p_{1/2}np;J=1$(a) series has larger widths and larger squared transition moments (1) than the 1(b) series. Note in part (a) of Table III the dramatic change in the resonance width between $n=10$ and 11 and the large value for $n=17$, $J=1$(a).

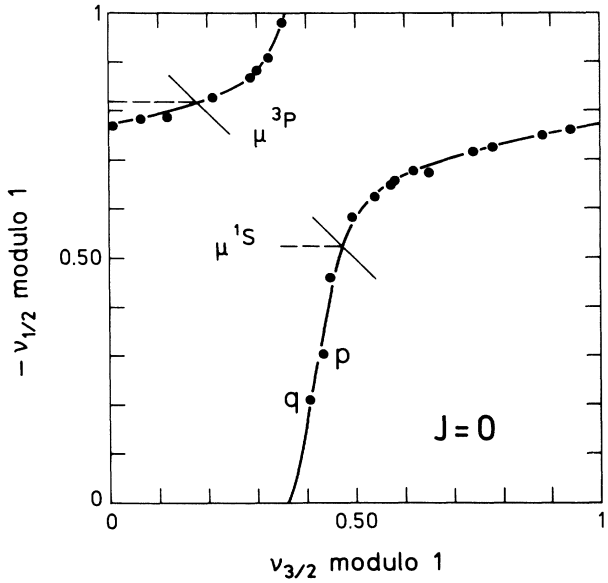

FIG. 4. Lu-Fano plot of the $-\nu_{1/2}$ (mod 1) quantum defect as a function of $\nu_{3/2}$ (mod 1) effective quantum number, for the $6p_{1/2}np;J=0$ and $6p_{3/2}n'p;J=0$ resonance states below the $6p_{1/2}$ limit. The $6p_{3/2}n'p;J$ states are labeled p ($n'=10$) and q ($n'=11$). The solid curve corresponds to the MQDT fit of Sec. IV B 1. A first estimate of μ^{1S} and μ^{3P} is obtained as the intersection of the curve with the $\nu_{1/2}=\nu_{3/2}$ (mod 1) diagonal.

3. $J=2$

The $6p_{1/2}np;J=2$ series in Table IV interacts with the two corresponding $6p_{3/2}n'p;J=2$(a) and 2(b) series. As mentioned above from the Lu-Fano plot in Fig. 6, the most perturbed state is that for $n=20$. The region of approximately constant $\nu_{1/2}$ determines $\delta_{1/2}^{J=2}=3.80$. The resonance width in Table IV roughly varies as $\nu_{1/2}^{-3}$, with $\Gamma\nu_{1/2}^{3}\simeq 5300$ cm^{-1}; the width for $n=17$ is larger, as in the case $J=1$(a).

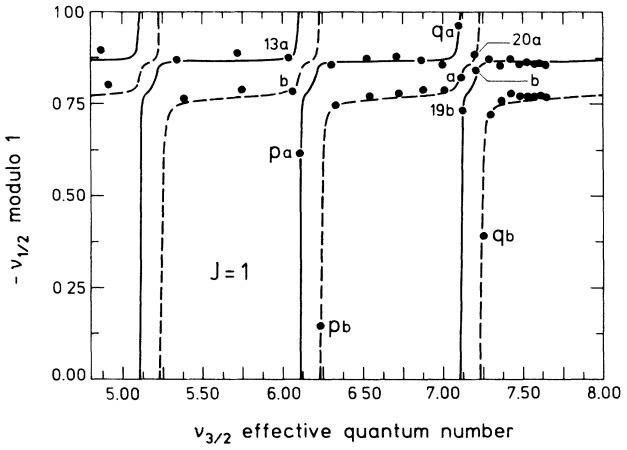

FIG. 5. Lu-Fano plot of the $-\nu_{1/2}$ (mod 1) quantum defect as a function of $\nu_{3/2}$ effective quantum number, for the $6p_{1/2}np;J=1$(a) and 1(b) and $6p_{3/2}n'p;J=1$(a) and 1(b) series below the $6p_{1/2}$ limit. In Figs. 5 and 6, the $6p_{3/2}n'p;J$(a) and J(b) states are labeled p_a and p_b ($n'=10$), q_a and q_b ($n'=11$). The solid curve corresponds to the MQDT fit of Sec. IV B 3. For each state, the deviation between measured and computed energies is smaller or of the order of the resonance width.

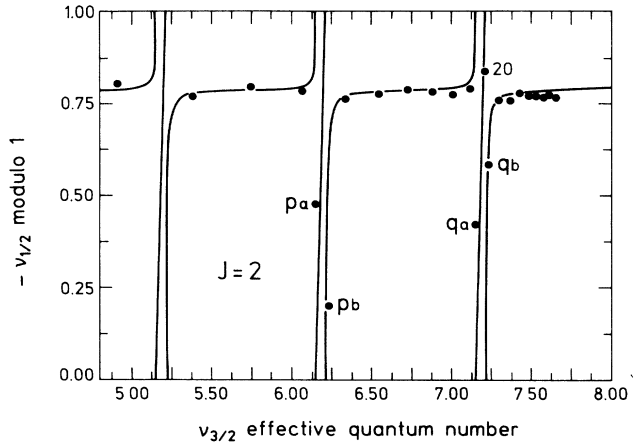

FIG. 6. Lu-Fano plot of the $-\nu_{1/2}$ (mod 1) quantum defect as a function of $\nu_{3/2}$ effective quantum number, for the $6p_{1/2}np;J=2$ and $6p_{3/2}n'p;J=2$(a) and 1(b) series below the $6p_{1/2}$ limit. The solid curve corresponds to the MQDT fit of Sec. IV B 2. For each state, the deviation between measured and computed energies is smaller or of the order of the resonance width. Note that the $n=20$ state is the most perturbed in the $6p_{1/2}np;J=2$ series.

B. The $6p_{3/2}np;J$ series

Apart from the $n=10$ and 11 multiplets below the $6p_{1/2}$ limit, the $6p_{3/2}np;J$ series appear as rather regular between $n=12$ and 28. In Table II, part (b) of Table III, and Table IV, one clearly checks the increase of the resonance widths across the $6p_{1/2}$ threshold. For instance, in the $J=0$ case, the width varies from 1.8 cm^{-1} ($n=11$) to 24 cm^{-1} ($n=12$). In the latter case, this is a clear indication that autoionization of the $6p_{3/2}np;J=0$ state mainly occurs in the $6p_{1/2}\epsilon l$ continuum. Actually, a preliminary attempt to measure the energy of the ejected electrons, by means of a time-of-flight analysis, has confirmed that autoionization of the $n=12$ multiplet predominantly occurs in the $6p_{1/2}\epsilon l$ continuum. The ordering of the energies within a given multiplet remains the same throughout the range $n=10$ to 28. It comes out, by order of increasing energies, as $J=1$(a), 2(a), 2(b), 1(b), and 0. No inversion is observed as it is often the case for the $6p_{1/2}np$ series. Specific remarks should be added, according to the different J values.

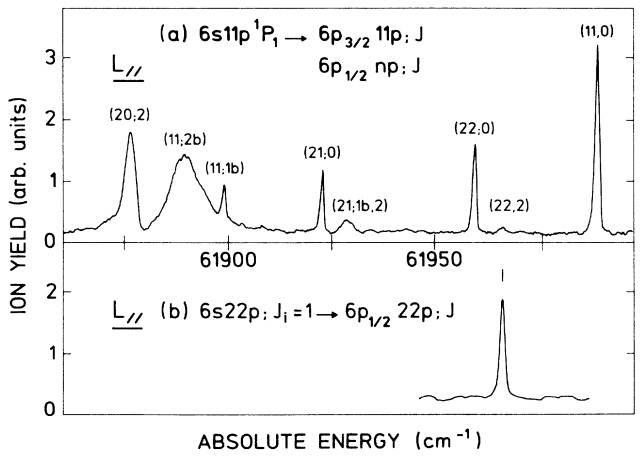

FIG. 7. Ba^+ ion yield as a function of λ_{II} wavelength (absolute energy scale), for $L_{\parallel}$ polarization. Spectrum (a): $6s11p\ ^1P_1 \rightarrow 6p_{3/2}11p;J$ excitation and $6s11p\ ^1P_1 \rightarrow 6p_{1/2}np;J$, $n=20,21,22$, indirect excitation. The corresponding structures are labeled $(n;J)$. Spectrum (b): $6s22p\ ^1P_1 \rightarrow 6p_{1/2}22p;J$ direct excitation.

1. $J=0$

For the $6p_{3/2}np;J=0$ series in Table II, the only series which can be thought of as a perturber is the $7sns;J=0$ series. However, its $7s^2$ lowest energy state is positioned according to the calculation of Aymar[17] at 65 000 cm^{-1}, that is above the $6p_{3/2}$ limit. Figure 8 displays the variation of the $\delta_{3/2}^{J=0}$ quantum defect for the $6p_{3/2}np;J=0$ series as a function of n principal quantum number. Surprisingly enough, whereas an essentially constant number is expected, the experimental points emphasize a regular increase, of about 0.2, of the quantum defect. In the same conditions, the quantum defects measured for the other $J=1$ and 2 series remain approximately constant, as shown in Fig. 8. Thus a systematic error due, for instance, to the energy calibration of the spectrum seems very unlikely. Story, Yap, and Cooke[11] have not reported such a regular variation of $\delta_{3/2}^{J=0}$. By the scale of the graph they have published, it is difficult to say whether their measurements agree with ours, or not. At present, we do not have a definite explanation for the variation observed. Because of the finite resonance

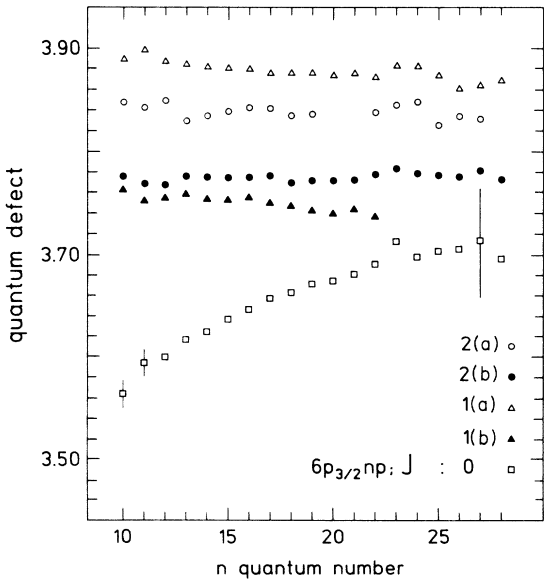

FIG. 8. Measured $\delta_{3/2}^{J}$ quantum defect for the $6p_{3/2}np;J$ series, as a function of n between 10 and 28. Note the variation of $\delta_{3/2}^{J=0}$; the error bars correspond to a 0.3 cm^{-1} uncertainty on the resonance energy. In the same conditions, quantum defects for $J=1$(a) and 1(b), $J=2$(a) and 2(b) series are approximately constant.

width, part of the variation may be attributed to a change in the resonance profile, with subsequent bias in the resonance energy [in particular, $(^1P,^3P)$ mixing takes place in the initial state—see Sec. IV]. However, according to the measured resonance widths, the shift should not exceed 0.002 for $n=10,11$, and a maximum of 0.04 for $n=12$. In Table II, the variation of the width with the $\nu_{3/2}$ effective quantum number is reasonably fitted by a $\nu_{3/2}^{-3}$ law, with $\Gamma\nu_{3/2}^3 \simeq 1.4\times10^4$ cm^{-1}. However, one notes the width for $n=23$, larger by a factor of 2 than the one expected.

2. $J=1$

Besides the $6p_{3/2}np;J=1$(a) series of lowest energy identified by Story, Yap, and Cooke in Ref. 11, we have measured the second $J=1$(b) state of the multiplet. As shown in part (b) of Table III and Fig. 8, the two series exhibit approximately constant quantum defects, 3.88 for the 1(a) series, in agreement with Ref. 11, and 3.75 for the 1(b) series. Actually, the second line was difficult to measure in our experimental conditions, as it probably was in the experiment of Story, Yap, and Cooke. The line has a small relative intensity for $n \leq 20$, and is hardly resolved from the stronger $J=2$(b) line for $n>20$. The variation of the resonance widths in part (b) of Table III is not fully regular. For the 1(a) series, a $\nu_{3/2}^{-3}$ law can only approximately fit the points $n=12$ to 19 ($\Gamma\nu_{3/2}^3 \simeq 3000$ cm^{-1}). For higher n, the widths remain significantly larger, by a factor of 2–3, than the fit-predicted values. Neither experimental uncertainty, nor limited resolution of the structure, entirely explains this deviation, since the 1(a) line is a well-isolated structure in the ion spectrum. The widths of 1(b) series are approximately fitted by the law $\Gamma\nu_{3/2}^3 \simeq 4500$ cm^{-1} in the range $n=12$ to 22. The width for $n=23$ significantly larger than the one predicted. For higher n values, measurements are affected by the limited resolution of the structure.

3. $J=2$

Energies and widths for the $6p_{3/2}np;J=2$(a) and 2(b) series are in Table IV. The two series present essentially constant quantum defects, 3.84 and 3.77, respectively, as shown in Fig. 8, in agreement with measurements in Ref. 11. The variation of the widths reproduces the same features as in the $J=0$ and 1 cases. For $n=12$ to 19, widths are approximately fitted as $\Gamma\nu_{3/2}^3$ of the order of 3000 cm^{-1} for 2(a), and 5500 cm^{-1} for 2(b). The widths for higher n are larger by a factor of 2–3 than the fit. The maximum values of the $\Gamma\nu_{3/2}^3$ product occur between $n=22$ and 24. This observation, common to all the $6p_{3/2}np;J$ series, can be partially related to the change in the character of the $6snp;J_i$ initial state between $n=21$ and 24, where ^1P and ^3P are mixed. However, a definite interpretation would require careful study of the resonance profile; this question is not addressed in the present work.

4. *Relative intensities within a multiplet*

The ratio of the total ion yields for two different J lines (the total ion yield is defined as the integrated signal under the resonance profile) is easily measured within a given n multiplet i.e., a given spectrum as in Fig. 3. The total ion yield ratios, $\mathcal{J}^{J=1(b)}/\mathcal{J}^{J=1(a)}$, from the $J=1$(b) to the 1(a) line, and $\mathcal{J}^{J=2(a)}/\mathcal{J}^{J=2(b)}$, from the $J=2$(a) to the 2(b) line, are plotted in Figs. 9 and 10, respectively, as a function of n. One notes that they present a maximum for $n=14,15$, and 23,24, where the ^1P and ^3P characters are mixed in the $6snp$ initial state; conversely, there is a minimum for $n=18$ to 20. As the ion yield measurements are sensitive to the symmetry of the initial state, they also reflect the symmetry of the quasibound final state. Hence we have attempted a qualitative test of the two limiting coupling schemes for describing the resonance state, either jj or jk, by comparing the simple computations of the transition moment in (1) to the experimental points. Within the ICE approximation, the transition moment is expressed as the product of three factors, i.e., an angular factor, the dipole matrix element for the ion core transition, and an overlap integral for the outer electron.[1] For achieving the computation, the bound part of the $6p_{3/2}np;J$ resonance state, for $J=1$ or 2, is expanded in either a jj- or a jk-coupled basis; the bases are, respectively,

$(6p_{3/2}npj_2';J)$, $j_2'=1/2,3/2$ for $J=1$ and 2,

$(6p_{3/2}np[k];J)$, $k=1/2,3/2$

for $J=1$; $3/2,5/2$ for $J=2$.

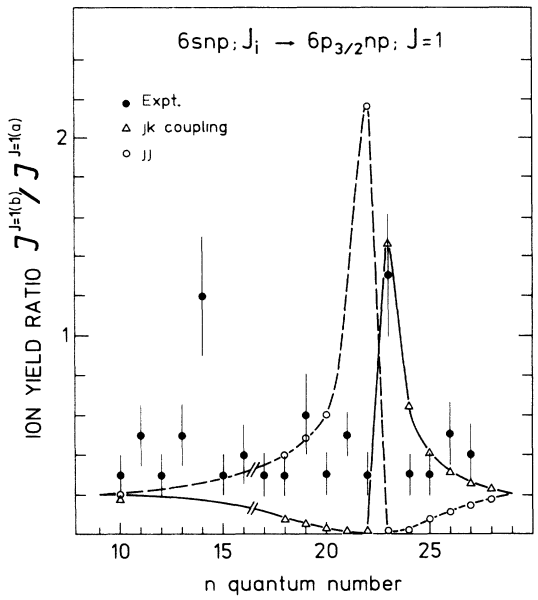

FIG. 9. Ratio of the $6p_{3/2}np;J=1$(b) to $J=1$(a) ion yields. ●, experimental points (measured for C_- polarization). △, computation from Sec. III B 4 for jk coupling in the asymptotic final state. The $(^1P,^3P)$ mixing in the $6snp;J_i$ state is accounted for between $n=18$ and 28; between 10 and 17, the solid line is only indicative. Qualitative agreement is obtained in the 18–28 interval, with resonance states labeled as 1(a), $k=3/2$ and 1(b), $k=1/2$. ○, the same for jj coupling in the asymptotic final state. Computed curve (or inverse) does not fit the experimental points.

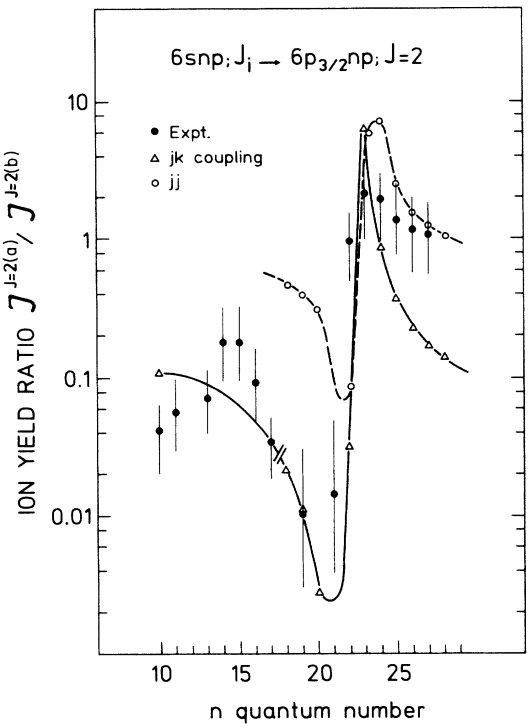

FIG. 10. Ratio of the $6p_{3/2}np;J=2$(a) to $J=2$(b) ion yields (the experimental points are measured for C_+ polarization). Comments are the same as in Fig. 9. For *jk* coupling, qualitative agreement is obtained with resonance states labeled as $J=2$(a), $k=5/2$ and $J=2$(b), $k=3/2$.

Now, the reduced transition moment in (1), for the $6snp;J_i \rightarrow 6p_{3/2}np;J$ transition, can be easily calculated under the following simplifying assumptions.

(i) The $6snp;J_i=1$ initial state is a linear combination of $^1P_1$ and $^3P_1$ *LS* states, with the mixing coefficients determined by Post, Vassen, and Hogervorst[16] for n between 18 and 28. (^1P,^3P) mixing should also exist for n between 11 and 15, but coefficients have not been measured until now.

(ii) Each of the two J(a) and J(b) resonance states is identified with one of its bound components in the above basis sets, either *jj* or *jk* coupled. The transition moment corresponds to the oscillator strength density integrated throughout the resonance profile.[18(a)]

Comparison between the measured and computed ratios is illustrated in Figs. 9 and 10. Although they are only grounded on a qualitative basis, at least two conclusions can be drawn from Figs. 9 and 10. First, the computation in the *jj*-coupling scheme does not reproduce the experimental points. Whether a ratio or its inverse is considered, it is impossible to check for both the position of the maxima and their order of magnitude (either the fit is off by one order of magnitude or the maxima are mismatched). Conversely, although it does not show full and accurate agreement, the computation in the *jk*-coupling scheme is certainly closer to the experimental points than the former one. Both the maximum for $n=23$ and the correct order of magnitude of the ratios are accounted for by the computation. Accordingly, a particular $6p_{3/2}np[k];J$ component should have a dominant weight in the long-range expansion of the resonance state. We find that the J components can be labeled, in order of increasing energy, $6p_{3/2}np[3/2];J=1$(a) and $J=2$(a), $[5/2];J=2$(b), $[1/2];J=1$(b), and $[1/2];J=0$. We note that this ordering, where components with the same k value are consecutive, is compatible with the energy structure of the *jk*-coupled multiplet. Finally, the measurement of ion yield ratios indicates that *jk*-coupling scheme is presumably better adapted than *jj* for describing the long-range symmetry and energy-level structure of the $6p_{3/2}np$ multiplet.

IV. ANALYSIS AND DISCUSSION

The purpose of this section is to develop a global and coherent analysis of the results on both $6p_{1/2}np;J$ and $6p_{3/2}np;J$ series, in the simplest possible frame. The choice of this simple frame is naturally suggested by the experimental results. First, the energy spacing between two consecutive multiplets (800 to 20 cm^{-1}, with increasing n) is always much larger than the resonance widths (20 to less than 1 cm^{-1}). Moreover, because of the finite laser linewidth, only partial measurements of the resonance widths were performed on the $6p_{1/2}np;J$ series. Therefore we have found it reasonable to limit our analysis to the energy positions of the resonances, without consideration of the widths. In this context, the dominant interaction for the $6p_{1/2}np;J$ and $6p_{3/2}np;J$ series is their mutual interaction below the $6p_{1/2}$ limit, as clearly illustrated by the Lu-Fano graphs in Figs. 4–6. Therefore we have restricted our analysis to the frame of the 6*pnp* configuration, below and above the $6p_{1/2}$ limit. However, we stress that comparison between the measured resonance energies and those from a discrete state model is only significant within the finite resonance widths.

A. Energy-level structure of the 6*pnp* configuration

In a first step, we have attempted to fit the energy-level structure of the 6*pnp* configuration, i.e., measured energies of both $6p_{1/2}np;J$ and $6p_{3/2}np;J$ series for $J=0$, 1, and 2, in terms of the six standard parameters:[18(b)] the ζ_{6p} and ζ_{np} spin-orbit integrals for the 6*p* and *np* electrons, respectively; the F^0,F^2 direct and G^0,G^2 exchange Slater integrals for electrostatic interaction. Our attempt partially repeats but further extends that reported in Ref. 11 in the case of the $6p_{3/2}15p$ multiplet. In Ref. 11, Story, Yap, and Cooke have limited their investigation to determining the four F^2, G^0, G^2, and ζ_{15p} parameters from the four energies they have measured [$J=0$, 1(a), 2(a), and 2(b)] in the multiplet. In our fit, we determine five parameters—ζ_{6p} is fixed, equal to 1127 cm^{-1}—including as experimental data, either (i) the five energies of the J components measured in the $6p_{3/2}np$ multiplet, or (ii) both sets of measured energies (four in $6p_{1/2}np$ and five in $6p_{3/2}np$ multiplets), that is a reasonably larger number of points than of parameters. The fit is repeated for different n values, between 16 and 23 in case (i), for

TABLE V. Parameters determined from analysis of the energy-level structure in the $6pnp$ configuration, for different n multiplets. (i) F^0, F^2 direct and G^0, G^2 exchange Slater integrals in cm^{-1}; n^* is the effective quantum number associated with $F^0_{(n)}$ average energy of the configuration. (ii) ζ_{np} spin-orbit integral in cm^{-1}.

n	F^0	n^*	F^2	G^0	G^2	ζ_{np}
16	62 686.7	12.20	49	7	9	2
17	62 794.2	13.20	38	4	6	1.5
18	62 879.9	14.21	29	3	3	1.5
19	62 949.0	15.23	25	2	2	
22	63 092.5	18.30	14	2	1	
23	63 125.6	19.30	10	1	1	

$n=16$, 17, 18, 22, and 23 in case (ii); in the latter case, the range of n values where the two multiplets strongly interact has been excluded. We have used for the fit the code displayed in Ref. 19. The Hamiltonian matrix (spin-orbit plus Coulomb interaction) is written in the LS-state basis for the $6pnp$ configuration. After diagonalization of the matrix, parameters are optimized so that energy eigenvalues fit the experimental data. Determinations of the different parameters are displayed in Table V. Calling n^* the effective quantum number associated with the average energy $F^0_{(n)}$ of the $6pnp$ configuration, we check that $F^2_{(n)}$ and $G^0_{(n)}$ vary approximately like $(n^*)^{-3}$.[18(c)] The determination of $G^2_{(n)}$ is affected by a larger uncertainty; its departure from a $(n^*)^{-3}$ law is not significant. The values of the ζ_{np} spin-orbit integral are between 1 and 2 cm^{-1} for $n=16$ to 18. This parameter could not be fixed for higher n. Finally, our results for $n=16$ to 23 are consistent with those in Ref. 11 for $n=15$. Spin-orbit interaction for the np electron is found, as expected, smaller than electrostatic interaction between the two electrons. This supports the conclusion of Sec. III B 4 that the jj-coupling scheme is not the best suited for describing the long-range symmetry of the resonance state. However, the contributions to the electrostatic energy of the direct and exchange Slater integrals, respectively, are found to be of the same order of magnitude (this can be checked further in the text from the energy expressions in Table VI); this somewhat contrasts with the condition (exchange terms negligible with respect to direct ones) which usually characterizes pure jk-coupling scheme.[20]

TABLE VI. Energies of the $LS;J$ states in the $6pnp$ configuration when spin orbit is ignored in terms of Slater integrals (Ref. 23). The μ^{1S} quantum defect is fixed from the Lu-Fano plot in Fig. 4. Other μ^{LS} associated to $E(LS)$ are estimated from (4) (μ^{LS} is averaged over the n multiplets in Table V).

$$E(^1P)=F^0-\frac{F^2}{5}-\left[G^0-\frac{G^2}{5}\right],\quad J=1,\quad \mu^{1P}=0.86$$

$$E(^3P)=F^0-\frac{F^2}{5}+\left[G^0-\frac{G^2}{5}\right],\quad J=0,1,2,\quad \mu^{3P}=0.79$$

$$E(^3D)=F^0+\frac{F^2}{25}-\left[G^0+\frac{G^2}{25}\right],\quad J=1,2,3,\quad \mu^{3D}=0.77$$

$$E(^1D)=F^0+\frac{F^2}{25}+\left[G^0+\frac{G^2}{25}\right],\quad J=2,\quad \mu^{1D}=0.69$$

$$E(^3S)=F^0+\frac{2F^2}{5}-\left[G^0+\frac{2G^2}{5}\right],\quad J=1,\quad \mu^{3S}=0.64$$

$$E(^1S)=F^0+\frac{2F^2}{5}+\left[G^0+\frac{2G^2}{5}\right],\quad J=0,\quad \mu^{1S}=0.53$$

B. MQDT analysis of $6pnp\,;J$ series

As mentioned, we deliberately limit our analysis to the energy positions of the resonances. With this restriction, MQDT analysis of the data involves the minimum number of channels required for a first-order positioning of the resonances, i.e., for a given J value, the $6p_{1/2}np\,;J$ and $6p_{3/2}np\,;J$ channels. Accordingly, resonances are viewed as bound states below the $6p_{1/2}$ limit; comparison with the measured resonance energies is only significant within the resonance widths. Our MQDT analysis makes use of the standard formulation of Lee and Lu,[21,22] developed in terms of the α eigenchannels. Since MQDT is an extensively documented topic in the literature, we only recall some particular points, which are relevant to the studied case. In the Lee and Lu formulation, two sets of channels are introduced, which are respectively appropriate to the limiting cases of short-range and long-range interaction between the electron and the core. The first set is that of the close-coupled α eigenchannels, which diagonalize the short-range interaction; the second set corresponds to the collision channels, labeled with an i index. The meaningful physical parameters are (i) the μ_α eigenquantum defects associated with the α eigenchannels, and (ii) the orthogonal U matrix, i.e., the transformation between the above two channel bases entering the description of the resonance state. In our simple model, the resonance energies below the $6p_{1/2}$ limit are discrete energies E which satisfy the following two well-known conditions:

$$E-E_i=-\frac{R}{\nu_i^2}\ , \tag{2}$$

$$F(\nu_i)=\det|U_{i\alpha}\sin\pi(\mu_\alpha+\nu_i)|=0\ , \tag{3}$$

where E_i is the ionization threshold associated with the collision channel i. In the case of $6pnp$ configuration, $\nu_{1/2}$ effective quantum number is expressed in (3) as a function of $\nu_{3/2}$; the corresponding curves are the Lu-Fano graphs in Figs. 4–6. Discrete state energies are at intersection with the curve from (2). It is a general assumption that in the short-range region, the electrostatic interaction dominates the spin-orbit interaction. As a result, the α eigenchannels have a dominant LS character. By neglecting spin-orbit terms in the short-range region, approximate values of the μ_α eigenquantum defects can be deduced from the energy-level structure of the $6pnp$ configuration, analyzed in Sec. IV A. In Table VI, we recall the expressions for the energies of the LS states in the $6pnp$ configuration, as a function of the Slater integrals.[23] The order in Table VI is that of increasing energy, as determined with the parameters of Table V. Now, the follow-

ing expression of the μ^{LS} eigenquantum defect is easily obtained, as a function of one of them, e.g., μ^{1S}:

$$\mu^{LS}=\bar{n}-\left[\frac{E_{(n)}(^1S)-E_{(n)}(LS)}{R}+\frac{1}{(\bar{n}-\mu^{1S})^2}\right]^{-1/2}, \quad (4)$$

where $\bar{n}$ is defined as the integer part of n^*+1 and equal to $n-3$. An estimate for μ^{1S}, $\mu^{1S}=0.53\pm0.01$, can be deduced from the Lu-Fano graph in Fig. 4 relative to the $6pnp$;$J=0$ series [one has made use of the rules (i) the μ_α eigenquantum defects are at intersection of the Lu-Fano graph from (3) with the diagonal $\nu_{1/2}=\nu_{3/2}$ (modulo 1),[21] and (ii) the $^1S_0$ state is the one of highest energy, i.e., of lowest quantum defect]. The μ^{LS} parameters determined by (4) turn out to be approximately constant, within 0.01, for the different n multiplets. Average values are given in Table VI.

As we mentioned in Sec. III B 4, the collision channel basis can be defined according to either the pure jj- or pure jk-coupling scheme. In that respect, we have noticed in Sec. III B 4 that jk coupling should be better adapted than jj for describing the bound part of the $6p_{3/2}np$;J resonance states in the long-range region. Hence, in our work, the U matrix is factorized in the form

$$U=T^J_{jk;LS}V\ , \quad (5)$$

where $T^J_{jk;LS}$ is the $(jk|LS)$ transformation within the $6pnp$;J configuration; the phase convention for $T^J_{jk;LS}$ is that of Ref. 18(d). The orthogonal V matrix accounts for the departure from pure LS coupling in the α eigenchannels.[21] V can be generated by successive rotations, each characterized by a $\beta_{\bar{\alpha}\alpha}$ angle (note that the order of the factors is not arbitrary):

$$V=\prod_{\bar{\alpha}<\alpha}R(\beta_{\bar{\alpha}\alpha})\ . \quad (6)$$

We have determined the energy-independent μ_α and $\beta_{\bar{\alpha}\alpha}$ parameters by fitting the measured resonance energies below the $6p_{1/2}$ limit. The fitting procedure uses the MQDTAC code developed by Robaux and Aymar.[24] In our case, the fit proceeds through minimization of the rms deviation between theoretical and experimental resonance energies, which are regarded as discrete state energies. Here, we should recall that the fit is essentially fixed by the points in the interaction zone of the Lu-Fano plot (for instance, of crucial importance is the curve profile in between the asymptotic branches), where only a limited number of them have been measured. Moreover, energies alone are often insufficient for determining a unique set of $\beta_{\bar{\alpha}\alpha}$ angles. An additional condition must be introduced, which consists in minimizing the deviation of V from the unity matrix. Actually, because of the limitations in the fit and of the approximations we made (ignoring open channels and limiting the analysis within the $6pnp$ configuration), the fit outputs—for instance, the $\beta_{\bar{\alpha}\alpha}$ angles and related quantities—should be interpreted with some care.

The wave function Ψ_E of the resonance state at energy E can be expanded in terms of the φ_i wave functions, in the jk-coupled collision channel basis:

$$\Psi_E=\sum_i Z_i\varphi_i\ . \quad (7)$$

The Z_i coefficients in (7) are easily calculated once the MQDT parameters are known. Of practical use is that Z_i^2 is proportional to the $\partial F/\partial\nu_i$ partial derivative of the $F(\nu_i)$ function in (3).[21] The coefficients relative to the jj-coupled basis are computed from the Z_i through a $(jk|jj)$ transformation. From both sets of coefficients, channel mixing is analyzed and the most appropriate labeling of the resonance state, in either the jk- or jj-coupling scheme, is selected. In the following, we consider percentage admixture coefficient $W_i=100Z_i^2$.

In order to check the consistency of the analysis below the $6p_{1/2}$ limit, we have extrapolated its predictions above threshold, and compared them with experimental data. For this, we refer to the alternative formulation of MQDT,[25–27] which makes use of the $\mathcal{R}$ short-range reactance matrix defined as $\mathcal{R}=U\tan(\pi\mu)^TU$. The determinantal equation (3) transforms into the equivalent one (3′), written in matrix form:

$$F(\nu_i)=\det(\mathcal{R}+\tan\pi\nu)=0\ . \quad (3')$$

Now, the ν_i parameters relative to the open channels are identified, modulo 1, to the $-\tau$ parameters, such that $\pi\tau$ are interpreted as eigenphase shifts in the open channels relative to the pure Coulomb phase, characteristic of the continuum eigenstates at energy E.[27] According to the increasing number of channels involved, the three analyses are presented in the order $J=0$, 2, and 1.

1. MQDT analysis of the 6pnp;J=0 series

Within the $6pnp$ configuration and $J=0$ subspace, the collision channels are the following, jk-coupled channels: channel 1,

$$6p_{1/2}np\,[1/2];J=0\ ,$$

channel 2,

$$6p_{3/2}np\,[1/2];J\ .$$

Note that they identically correspond to the $6p_{1/2}np_{1/2}$;$J=0$ and $6p_{3/2}np_{3/2}$;$J=0$, jj-coupled channels, respectively. The two α eigenchannels can be labeled according to their dominant LS character: α eigenchannel 1, $^1S_0$; and 2 $^3P_0$. The μ_α eigenquantum defects obtained from the fit are in Table VII. They are compatible, within 0.02, with their estimated value from (4). The fit does not introduce significant deviation of the U matrix from its initial $T^{J=0}_{jk;LS}$ determination; the β_{12} angle is fixed to -0.07 rad. The corresponding graph is displayed in Fig. 4. The deviation between the measured and computed energies is smaller or of the order of the

TABLE VII. μ_α eigenquantum defects labeled according to the dominant LS character of the α eigenchannels. Row 1, reproduced from Table VI, i.e., determined from analysis of the energy-level structure in the $6pnp$ configuration. Rows 2–4, estimated from MQDT fit on the $6P_{1/2,3/2}np\,;J$ series.

Method	^1S	^3S	^1D	^3D	^3P	^1P
$6pnp$ configuration	0.53	0.64	0.69	0.77	0.79	0.86
MQDT fit						
$J=0$	0.53				0.81	
$J=1$		0.72		0.86	0.81	0.91
$J=2$			0.74	0.81	0.85	

resonance width.

The strong interaction between the two series is reflected by the mixing of the $6p_{1/2}np\,[1/2];J=0$ and $6p_{3/2}n'p\,[1/2];J=0$ states ($n'=9,10,11$) in the wave function (7) of the $6pnp\,;J=0$ resonance state. The $W_{1/2,3/2}$ percentage admixture coefficients are listed in Table VIII. One notes the significant weight of the $6p_{3/2}n'p\,[1/2];J$ channel in the $6p_{1/2}np\,;J$ state, for $n=11$, 14, 15, and 21–24. This important channel mixing explains that it is possible to excite the $J=0$ component of the $6p_{1/2}np$ multiplet, starting from the $6sn'p\ ^1P_1$, $n'=10$ or 11, initial state, as was observed in spectrum (a) in Fig. 7.

Extrapolation above the $6p_{1/2}$ limit. The extrapolation of the previous analysis above the $6p_{1/2}$ limit is, obviously, only indicative. It proceeds from our assumption that the dominant coupling for the $6p_{3/2}np\,;J$ states is with the $6p_{1/2}\epsilon p\,;J$ open channel, the other ones being ignored. Above the $6p_{1/2}$ limit, $\pi\nu_{1/2}$ corresponds to the eigenphase shift in the unique open channel. This phase shift varies by π with energy when crossing a resonance in the closed channel, i.e., $T_1=\tan\pi\nu_{1/2}$ should have a pole for the resonance energy.[25,27] According to the simple form (3′) of the determinantal equation, poles of T_1 occur for $\nu_{3/2}=(1/\pi)\arctan(-\mathcal{R}_{22})$ (mod 1), which corresponds to a quantum defect of 0.54. We note that this value is roughly compatible with the lowest measured value of the quantum defect for the $6p_{3/2}np\,;J=0$ series in Table II, $\delta_{3/2}^{J=0}=0.56$ for $n=10$.

TABLE VIII. Percentage admixture coefficients, $W_i=100Z_i^2$, of the $6P_{1/2}np\,[1/2];J$ and $6p_{3/2}np\,[1/2];J$ collision channels in the $6p_{1/2,3/2}np\,;J=0$ resonance states below the $6p_{1/2}$ limit. W_i are computed using MQDT parameters from the fit in Sec. IV B 1. In Tables VIII–X, the $6p_{1/2,3/2}np\,[k];J$ channels are noted 1/2,3/2[k].

$J=0$	1/2[1/2] W_1	3/2[1/2] W_2
$6p_{1/2}10p$	93	7
$6p_{1/2}11p$	60	40
$6p_{3/2}9p$	3	97
$6p_{1/2}12p$	94	6
$6p_{1/2}13p$	95	5
$6p_{1/2}14p$	78	22
$6p_{3/2}10p$	44	56
$6p_{1/2}15p$	89	11
$6p_{1/2}np$ $16\le n\le 20$	>95	
$6p_{1/2}21p$	93	7
$6p_{1/2}22p$	84	16
$6p_{3/2}11p$	79	27
$6p_{3/2}23p$	81	19
$6p_{3/2}24p$	92	8
$6p_{1/2}np$ $n\ge 25$	>95	

2. The 6pnp;J=2 series

Our simple analysis of the $6p_{1/2,3/2}np\,;J=2$ series is developed in the three, jk-coupled, collision channel basis: channel 1,

$$6p_{1/2}np\,[3/2];J\ ,$$

channel 2,

$$6p_{3/2}np\,[3/2];J\ ,$$

channel 3,

$$6p_{3/2}np\,[5/2];J\ .$$

The three α eigenchannels are labeled according to their dominant LS character: α eigenchannel 1, $^1D_2$; 2, $^3D_2$; 3, $^3P_2$. From analysis of Sec. IV A, we have associated with each of them in Table VI a first determination of the μ_α eigenquantum defects. The μ_α parameters obtained from the fit are reported in Table VII. They are systematically larger, by about 0.06, than the ones initially determined. The $\mu^{^3P}$ parameter is also slightly larger (+0.03) than the one determined in the fit for $J=0$. The V matrix (6) is a product of three rotation matrices; $\beta_{\bar\alpha\alpha}$ angles estimated from the fit are, in radians, $\beta_{12}=-0.01$, $\beta_{13}=-0.20$, and β_{23} not significantly different from zero.

We find that jk coupling is better adapted than jj for describing the resonance states in the long-range region. The W_i admixture coefficients in the $6p_{1/2}np\,;J$ and $6p_{3/2}np\,;J$ resonance states below the $6p_{1/2}$ limit are listed in Table IX. All the states but the $6p_{1/2}20p\,;J=2$ and the $6p_{3/2}11p\,;J=2$(b) states have W_i weight larger than 95 in the jk-coupled basis. The jk labeling of the $6p_{3/2}n'p\,;J$ resonance states, $n'=9,10,11$ proceeds from Table IX as $k=3/2$ for 2(a) resonance and $k=5/2$ for 2(b) resonance. It is compatible with that for the $J=2$ resonance states, deduced above threshold from the analysis of ion yield ratios in Sec. III B 4.

One checks that the $6p_{1/2}np\,;J=2$ series is much less perturbed than the $J=0$ series, since only the $6p_{1/2}20p\,;J=2$ state has an appreciable $6p_{3/2}np\,[k];J$ component ($W_3=26$ for $k=5/2$). This explains why the $6p_{1/2}20p\,;J=2$ state is efficiently excited from the $6s11p\ ^1P_1$ state [in spectrum (a) in Fig. 7], whereas other

TABLE IX. Percentage admixture coefficients, $W_i=100Z_i^2$, of the $6p_{1/2}np[k];J$ and $6p_{3/2}np[k];J$ collision channels in the $6p_{1/2,3/2}np;J=2$ resonance states below the $6p_{1/2}$ limit. W_i are computed using MQDT parameters from the fit in Sec. IV B 2. See Table VIII.

$J=2$	1/2[3/2] W_1	3/2[1/2] W_2	3/2[5/2] W_3
$6p_{1/2}np$ $n\neq 20$	>96		
$6p_{3/2}10p$ (a)	1	99	
$6p_{3/2}10p$ (b)	5		95
$6p_{3/2}11p$ (a)	3	97	
$6p_{1/2}20p$	74		26
$6p_{3/2}11p$ (b)	31		69

members of the same series ($n=21,22$) are not as easily accessible.

Extrapolation above the $6p_{1/2}$ limit. Keeping in mind that our three-channel analysis can provide but only a rough description of the continuum above the $6p_{1/2}$ limit, we nevertheless attempt an extrapolation to check the consistency of our treatment. As we recall from Sec. IV B 1, with collision channel 1 becoming open, $\pi\nu_{1/2}$ corresponds to the eigenphase shift of the one-dimensional continuum; $\pi\nu_{1/2}$ varies by π, i.e., T_1 has poles, across the resonances in the closed channels. From (3'), we obtain the expression of T_1 as a function of T_2 and T_3, where $T_i=\tan\pi\nu_i$:[27]

$$T_1+\mathcal{R}_{11}=\frac{\mathcal{R}_{13}^2(T_2+\mathcal{R}_{22})+\mathcal{R}_{12}^2(T_3+\mathcal{R}_{33})-2\mathcal{R}_{12}\mathcal{R}_{13}\mathcal{R}_{23}}{(T_2+\mathcal{R}_{22})(T_3+\mathcal{R}_{33})-\mathcal{R}_{23}^2}\ . \tag{8}$$

Since the two closed channels have the same $6p_{3/2}$ limit, we have $T_2=T_3$; the poles of T_1 are obtained as the roots $T_\pm$ of the denominator in (8) [the cofactor of $T_1+\mathcal{R}_{11}$ in the determinant (3') should be zero]:

$$T_\pm=\tfrac{1}{2}\{-\mathcal{R}_{22}-\mathcal{R}_{33}\pm[(\mathcal{R}_{22}-\mathcal{R}_{33})^2+4\mathcal{R}_{23}^2]^{1/2}\}\ . \tag{9}$$

$T_\pm$ correspond to the two $J=2$(b) and 2(a) resonance states, respectively. The quantum defects of the autoionizing series are $\delta_{3/2}^{J=2(a)},\delta_{3/2}^{J=2(b)}=1-(1/\pi)\arctan(T_\mp)$, $0\leq\arctan(T_\mp)<\pi$; they are equal to 0.85 to 0.77, which values reasonably agree with the ones experimentally measured in Table IV and Fig. 8. The unique continuum eigenstate at energy E has an expansion (7) in the long-range region; one easily expresses from (3') the ratio of admixture coefficients relative to the closed channels:

$$\frac{W_2}{W_3}=\frac{\partial F(\nu_i)/\partial\nu_2}{\partial F(\nu_i)/\partial\nu_3}=\frac{1+T_2^2}{1+T_3^2}\frac{(T_3+\mathcal{R}_{33})(T_1+\mathcal{R}_{11})-\mathcal{R}_{13}^2}{(T_2+\mathcal{R}_{22})(T_1+\mathcal{R}_{11})-\mathcal{R}_{12}^2}=\frac{T_\pm+\mathcal{R}_{33}}{T_\pm+\mathcal{R}_{22}}\ . \tag{10}$$

The latter simplified form is obtained at resonance energy, where $T_2=T_3=T_\pm$ and T_1 infinite (the two ratios for T_+ and T_-, respectively, are inverse of each other). With the estimated parameters [$\mathcal{R}_{23}\simeq 10^{-3}$, much smaller than $\mathcal{R}_{22}$ and $\mathcal{R}_{33}$ in (9), so that $T_{+(-)}\simeq-\mathcal{R}_{33(22)}$], the ratio (10) varies from a few 10^{-3} [T_+; resonance 2(b)] to more than 100 [T_-; resonance 2(a)]. This noticeable contrast shows that the $6p_{3/2}np;J=2$ states are well described in the long-range region by almost pure jk coupling [$k=5/2$ for 2(b) resonance, and $k=3/2$ for 2(a)]. The latter assignment is consistent with that obtained for $6p_{3/2}np;J=2$ states located below the $6p_{1/2}$ limit. It is also compatible with the jk labeling of $6p_{3/2}np;J=2$ states deduced above threshold in Sec. III B 4.

3. *The 6pnp;J=1 series*

Our MQDT analysis of the $6p_{1/2,3/2}np;J=1$ series is developed in the basis of the following four, jk-coupled collision channels: channel 1,

$$6p_{1/2}np[1/2];J\ ,$$

channel 2,

$$6p_{1/2}np[3/2];J\ ,$$

channel 3,

$$6p_{3/2}np[1/2];J\ ,$$

channel 4,

$$6p_{3/2}np[3/2];J\ .$$

The α eigenchannels, labeled according to their dominant LS character, are α eigenchannel 1 $^3S_1$; 2, $^3P_1$; 3, $^1P_1$; 4, $^3D_1$. A first determination of the μ_α eigenquantum defects has been attached to the α eigenchannels in Table VI. The μ_α parameters estimated in the fit are reported in Table VII. The $\mu^{^3S}$ and $\mu^{^1P}$ are larger (by 0.06 and 0.04, respectively) than their determinations in Table VI. Another observation is that $\mu^{^3D}$ and $\mu^{^3P}$ have inverted their relative magnitude with respect to the $J=2$ fit. Actually, the determinations of $\mu^{^3D}$ and $\mu^{^3P}$ in Sec. IV A, resulting from the global analysis of the $6pnp$ configuration, are close to each other, within 0.02 rad. The V matrix in (6) is the product of six rotations; $\beta_{\bar\alpha\alpha}$ angles determined in the fit are, in radians, as follows: β_{12}, 0.07; β_{13}, −0.18; β_{14}, 0.10; β_{23}, −0.17, β_{24}, 0.00; β_{34}, 0.04. The corresponding graph displayed in Fig. 6 is already satisfactory. The deviation between the experimental and computed energies is smaller or of the order of the widths; the inflection of the curves in between their asymptotic parts is generated and should be significant.

The W_i admixture coefficients in the $6p_{1/2}np;J$ and $6p_{3/2}n'p;J$ resonance states below the $6p_{1/2}$ limit are computed in Table X, relative to the jk-coupled basis. Although the perturbation of the $6p_{1/2}np;J=1$ series by the $6p_{3/2}n'p;J$ states is stronger than for the $J=2$ series, it significantly affects only a limited number of states. Far from the perturbers ($n\neq 13,19,20$), the $6p_{1/2}np;J=1$(a) and 1(b) states are well described in ei-

ther the *jk*- or *jj*-coupling scheme, with in both cases dominant weight, $W_i > 95$, of a purely coupled state. In the perturbed energy ranges ($n = 13,19,20$), the series interaction induces a very irregular variation of the W_i coefficients, when going from one to the following n state. For these states, although by a small percentage, the *jk*-coupling scheme is, again, better adapted than the *jj*. From Table X the $6p_{3/2}n'p;J$ resonance states below threshold are approximately labeled as $k=3/2$ for 1(a) resonance and $k=1/2$ for 1(b) resonance. This labeling is consistent with that derived above threshold from ion yield ratio analysis in Sec. III B 4.

In the three fits for $J=0$, 2, and 1, we have noted that the successive determinations of the μ_α parameter, for a given *LS* character of the α eigenchannel, can be significantly different. This should reflect a deviation from pure *LS* coupling in the α eigenchannels (for pure *LS* coupling, the μ_α parameter is independent of *J*). Moreover, some of the $\beta_{\bar{\alpha}\alpha}$ angles have reached finite values between 0.1 and 0.2 rad, which account for the same deviation. However, part of the deviation observed in the fits must be certainly attributed to the limitations of our analysis (the limited amount of data, simplified analysis, and numerical procedure) evoked in the beginning of Sec. IV B.

Extrapolation above the $6p_{1/2}$ limit. Extrapolation above the $6p_{1/2}$ limit is analogous to that in the $J=2$ case. Channels 1 and 2 becoming open, the continuum at a given energy E is a two-dimensional subspace generated by the $\psi_{E,\tau}$ and $\psi'_{E,\tau'}$ eigenstates. The eigenphase shifts in the open channels, τ and τ', are the two roots of Eq. (3'), where we have set $\nu_1=\nu_2=-\tau$ or $-\tau'$ (mod 1) in the 4×4 determinant. The resonances occur where $\pi\tau$ or $\pi\tau'$ varies rapidly by π, i.e., where $\tan\pi\tau$ has poles. Accordingly, it is easy to see that the coefficient of $(\tan\pi\tau)^2$ in (3') should be zero; this corresponds to

$$(T_3+\mathcal{R}_{33})(T_4+\mathcal{R}_{44})-\mathcal{R}_{34}^2=0\ . \tag{11}$$

Since the closed channels 3 and 4 have the same limit, the two 1(b) and 1(a) resonances are associated with the $T_\pm$ roots of (11) where $T_3=T_4$, as in the $J=2$ case. We find the quantum defects $\delta_{3/2}^{J=1(a)}$ and $\delta_{3/2}^{J=1(b)}$, given by $1-(1/\pi)\arctan(T_\mp)$, equal to 0.89 and 0.75, respectively. They reasonably compare with the experimental values in part (b) of Table III and Fig. 8. An analogous computation to that in Sec. IV B 2 gives the W_3/W_4 ratio of the weights of the closed channels in the $\psi_{E,\tau}$ and $\psi'_{E,\tau'}$ eigenstates. The ratio is the same for both eigenstates and we have, at resonance (T_1 and T_2 infinite; $T_3=T_4=T_\pm$), the same type of expression as (10):

$$\frac{W_3}{W_4}=\frac{T_\pm+\mathcal{R}_{44}}{T_\pm+\mathcal{R}_{33}}\ , \tag{12}$$

giving 6.8 for the 1(b) resonance and inverse 0.15 for the 1(a). This contrast is not as pronounced as in the $J=2$ case in Sec. IV B 2. However, it shows that the $6p_{3/2}np;J=1$ states above threshold still have a dominant, specific *jk* character [$k=1/2$ for 1(b) resonance and 3/2 for 1(a)]. This assignment is consistent with that below threshold from Table X; one checks that it is the same as the one deduced above threshold in Sec. III B 4.

Finally, in the three *J* cases which have been considered, we have consistently concluded that *jk* coupling is better adapted than *jj* for describing the long-range symmetry of the $6p_{1/2,3/2}np;J$ resonance states. In the $6p_{3/2}np;J$ case, this was independently supported, on the one hand, by the ion yield ratio analysis in Sec. III B 4, and on the other hand, by the MQDT analysis of the $6p_{1/2,3/2}np;J$ series. Evidence from the ion yield analysis was not as marked in the $6p_{1/2}np;J$ case, where neither simple computation in *jk* nor in *jj* coupling fits fully the measured quantities. In this case, where an important channel mixing is involved for most of the n values, further development is probably required.

TABLE X. Percentage admixture coefficients, $W_i=100Z_i^2$, of the $6p_{1/2}np[k];J$ and $6p_{3/2}np[k];J$ collision channels in the $6p_{1/2,3/2}np;J=1$ resonance states below the $6p_{1/2}$ limit. W_i are computed using MQDT parameters from the fit in Sec. IV B 3. See text. See Tables VIII and IX.

$J=1$	1/2[1/2] W_1	1/2[3/2] W_2	3/2[1/2] W_3	1/2[3/2] W_4
$6p_{1/2}np$ (a) $n\neq13,19,20$		>96		
$6p_{1/2}np$ (b) $n\neq13,19,20$	>94			
$6p_{1/2}13p$ (a)	7	90	1	2
$6p_{1/2}13p$ (b)	84	9	4	34
$6p_{3/2}10p$ (a)	8	1	7	84
$6p_{3/2}10p$ (b)	10		80	10
$6p_{3/2}11p$ (a)	18	21	8	53
$6p_{1/2}19p$ (a)	9	78	2	11
$6p_{1/2}19p$ (b)	74	1		25
$6p_{1/2}20p$ (a)	15	81	2	2
$6p_{1/2}20p$ (b)	68	18	11	3
$6p_{3/2}11p$ (b)	26		67	7

V. CONCLUSION

We have used the $6s^2\,{}^1S_0\rightarrow6snp\,{}^1P_1\rightarrow6p_{1/2,3/2}np;J$ scheme of isolated core excitation for investigating energy positions, widths, and transition moments associated with the $6p_{1/2}np;J$ and $6p_{3/2}np;J$ autoionizing states with $J=0$, 1, and 2, for n between 10 and 28. This represents nine of the ten series of the $6pnp$ configuration, the $J=3$ series being excepted. The results on the $6p_{3/2}np;J$ series are in general agreement with those of Story, Yap, and Cooke in Ref. 11. The extended set of experimental results has allowed us to develop simple and complementary analyses, providing a comprehensive view of the $6pnp$ configuration: successively, the energy-level structure of the $6pnp$ multiplet, and the interaction of the $6p_{1/2}np;J$ and $6p_{3/2}np;J$ series studied within a simple MQDT model, have been considered. We find that *jk* coupling should be the best suited for describing the long-range symmetry of the $6p_{1/2,3/2}np;J$ resonance states. However, it is fair to say that this conclusion may depend on the approximation made throughout the mod-

el, that the resonance state can be represented within the only $6pnp$ configuration. This approximation is certainly questionable in our MQDT treatment below $6p_{1/2}$ limit, neglecting all open channels as well as $6pnf$ configuration, therefore reducing channel mixing in the long-range region. Moreover, MQDT analysis rests on the resonance energies alone, and may be insufficient for an accurate determination of the resonance state wave functions. Although they are grounded on consistent arguments, our conclusions may slightly vary on account of further investigations. Careful analysis of the resonance widths and transition moments should be pursued, allowing a definite comparison with *ab initio* calculations, e.g., of the R-matrix type. Work is in progress in that sense.

ACKNOWLEDGMENTS

The authors have the pleasure to thank Dr. A. L'Huillier for her kind assistance in the computer work, and Dr. M. Poirier for helpful discussions.

[1]E. Y. Xu, Y. Zhu, O. C. Mullins, and T. F. Gallagher, Phys. Rev. A **33**, 2401 (1986).
[2]R. R. Jones, C. J. Dai, and T. F. Gallagher, Phys. Rev. A **41**, 316 (1990).
[3]U. Eichmann, P. Brockmann, V. Lange, and W. Sandner, J. Phys. B **22**, L361 (1989).
[4]E. A. J. M. Bente and W. Hogervorst, J. Phys. B **22**, 2679 (1989).
[5]W. Sandner, U. Eichmann, V. Lange, and M. Völkel, J. Phys. B **19**, 51 (1986).
[6]J. Boulmer, P. Camus, and P. Pillet, J. Opt. Soc. Am. B **4**, 805 (1987).
[7]P. Camus, T. F. Gallagher, J.-M. Lecomte, P. Pillet, L. Pruvost, and J. Boulmer, Phys. Rev. Lett. **62A**, 2365 (1989).
[8]R. R. Jones and T. F. Gallagher, Phys. Rev. A **38**, 2846 (1988).
[9]W. E. Cooke, T. F. Gallagher, S. A. Edelstein, and R. M. Mill, Phys. Rev. Lett. **40**, 178 (1978).
[10]F. Gounand, T. F. Gallagher, W. Sandner, K. A. Safinya, and R. Kachru, Phys. Rev. A **27**, 1925 (1983).
[11]J. G. Story, E. G. Yap, and W. E. Cooke, Phys. Rev. A **39**, 5127 (1989).
[12]S. M. Jaffe, R. Kachru, H. B. Van Linden van den Heuvell, and T. F. Gallagher, Phys. Rev. A **32**, 1480 (1985).
[13]J. A. Amstrong, J. J. Wynne, and P. Esherick, J. Opt. Soc. Am. **69**, 211 (1979). See also highly accurate values for $n>15$ in B. H. Post, W. Vassen, W. Hogervorst, M. Aymar, and O. Robaux, J. Phys. B **18**, 187 (1985).
[14]N. Pelletier-Allard and R. Pelletier, Rev. Sci. Instrum. **55**, 1442 (1984).
[15]A. Yu. Elizarov and N. A. Cherepkov, Zh. Eksp. Teor. Fiz. **96**, 1224 (1989) [Sov. Phys.—JETP **69**, 695 (1989)].
[16]B. H. Post, W. Vassen, and W. Hogervorst, J. Phys. B **19**, 511 (1986).
[17]M. Aymar, J. Phys. B **22**, 2359 (1989).
[18](a) R. D. Cowan, *The Theory of Atomic Structure and Spectra* (University of California Press, Berkeley, 1981), p. 525; (b) *ibid.*, pp. 163 and 216; (c) *ibid.*, p. 228; (d) *ibid.*, p. 249.
[19]Y. Bordarier, A. Bachelier, and J. Sinzelle, codes DIAGAC and GRAMAC, Laboratorie Aimé Cotton (unpublished).
[20]D. E. Kelleher and E. B. Saloman, Phys. Rev. A **35**, 3327 (1987), p. 3329.
[21]C. M. Lee and K. T. Lu, Phys. Rev. A **8**, 1241 (1973).
[22]U. Fano, Phys. Rev. A **2**, 353 (1970).
[23]E. V. Condon and G. H. Shortley, *Theory of Atomic Spectra* (Cambridge University Press, London, 1963), p. 199.
[24]O. Robaux and M. Aymar, Comput. Phys. Commun. **25**, 223 (1982).
[25]M. J. Seaton, Rep. Prog. Phys. **46**, 167 (1983).
[26]A. Giusti-Suzor and U. Fano, J. Phys. B **17**, 215 (1984).
[27]W. E. Cooke and C. L. Cromer, Phys. Rev. A **32**, 2725 (1985).